



A scalable method for estimating rooftop solar irradiation potential over large regions

René Buffat*, Stefano Grassi, Martin Raubal

Institute of Cartography and Geoinformation, ETH Zurich, 8093 Zurich, Switzerland



HIGHLIGHTS

- Scalable method to estimate building rooftop solar irradiation potential.
- Validation of monthly energy production of 500 PV systems in Switzerland: $R^2 = 0.9$.
- Median error in July -0.55% , in December $+28.08\%$ (probably due to snow cover).
- The model shows for Switzerland a rooftop PV potential of 53.2 TW h.

ARTICLE INFO

Keywords:

Rooftop solar irradiation estimation
Spatio-temporal modelling
Geographic information systems (GIS)
Big data

ABSTRACT

An estimate of solar irradiation potential over large regions requires the knowledge of the long-term spatio-temporal distribution of the solar radiation as well as the identification of the suitable surfaces where the photovoltaic (PV) installations can be built. These main components can be modelled in different ways and are thus affected by different sources of uncertainty. Thus, when estimating the exploitable potential over large regions, it is important to measure the accuracy of the entire process. In this work, we provide a generic method to estimate the solar irradiation potential of rooftops over large regions and an estimate of the corresponding uncertainties when calculating the long-term electricity generation of PV plants. This method uses satellite based solar radiation data covering a period of 22 years, with a temporal resolution of 30 min and a spatial resolution of 3.8–5.6 km. Suitable surfaces on rooftops are identified using Digital Surface Models combined with building footprints. This allows to determine the geometry of rooftops, such as slope, and orientation with a spatial resolution of 0.5 m. Finally, we calculated the electricity generation based on models which take into account all characteristics of PV system components. In order to estimate the accuracy of the model for electricity production, we compared the monthly generation of 500 PV plants in Switzerland consisting of different PV technologies (mono-crystalline, poly-crystalline and thin film) with the estimates. The validation results show a correlation coefficient (R^2) of 0.9 and a median monthly relative error between 0.28% (August) and 28.08% (December). The monthly estimates are more accurate during summer time, while spatially and technology-wise no significant differences are found.

1. Introduction

The modelling and prediction of the spatio-temporal solar irradiation is a challenging task due to the complexity and variability of the involved phenomena. The amount of solar irradiation reaching the surface of the Earth is subject to cloud cover and the composition of solar irradiation in the atmosphere [1], the slope and orientation of tilted surfaces, shadows due to local natural and anthropogenic objects [2] and the reflectance properties of the ground.

Photovoltaic (PV) systems transform the incoming solar irradiance to electricity and consist of several electrical components, such as PV

modules and inverters whose performance is affected by multiple exogenous and endogenous factors. The transformation efficiency of such systems depends on the physical properties of the used components, such as the performance of the PV cell or the inverter, but also environmental properties such as dusting, external temperature and the level of solar irradiance [3]. For these reasons, when estimating the PV potential, the critical main aspects to consider are (1) the assessment of the accuracy of both the data of the solar radiation over the time and over the space and (2) the model transforming the solar radiation into electricity using PV systems.

Concerning the solar radiation, at present there are two main

* Corresponding author.

E-mail address: rbuffat@ethz.ch (R. Buffat).

Nomenclature

α	orientation of inclined surface	$G_{R,\alpha,\beta}$	reflected solar irradiance on inclined surface $\left[\frac{\text{W}}{\text{m}^2}\right]$
α_{ISC}	temperature coefficient of short circuit current	I_m	solar irradiation of month m [Wh]
β	slope of inclined surface	I_s	diode saturation current of the single-diode model
β_{VOC}	temperature coefficient of open circuit voltage	I_{MP}	current at maximum power point
ρ	ground reflectance albedo	I_{ph0}	diode photo current of the single-diode model at NOCT conditions
θ_h	solar elevation angle [rad]	I_{ph}	diode photo current of the single-diode model
θ_i	incidence angle on inclined surface [rad]	I_{s0}	diode saturation current of the single-diode model at NOCT conditions
θ_z	solar zenith angle [rad]	I_{SC}	current at short circuit condition
θ_{hor}	horizon angle [rad]	k	Boltzman constant
a	diode ideality factor of the single-diode model	<i>mono</i>	mono-crystalline PV cell technology
a_0	diode ideality factor of the single-diode model at NOCT conditions	N_p	number of cells of a PV module in parallel
A_{cell}	PV cell area	N_s	number of cells of a PV module in series
A_{panel}	PV panel area	<i>NOCT</i>	nominal operation cell temperature
E_g	energy gap	<i>poly</i>	poly-crystalline PV cell technology
<i>FF</i>	fill factor	q	elementary charge
G	global horizontal solar irradiance $\left[\frac{\text{W}}{\text{m}^2}\right]$	R_s	series resistance of the single-diode model
G_B	direct horizontal solar irradiance $\left[\frac{\text{W}}{\text{m}^2}\right]$	R_{s0}	series resistance of the single-diode model at NOCT conditions
G_D	diffuse horizontal solar irradiance $\left[\frac{\text{W}}{\text{m}^2}\right]$	R_{sh0}	shunt resistance of the single-diode model at NOCT conditions
$G_{\alpha,\beta}$	global solar irradiance on inclined surface $\left[\frac{\text{W}}{\text{m}^2}\right]$	R_{sh}	shunt resistance of the single-diode model
$G_{B,\alpha,\beta}$	direct solar irradiance on inclined surface $\left[\frac{\text{W}}{\text{m}^2}\right]$	T_{ref}	nominal operating PV cell temperature
$G_{D,\alpha,\beta}$	diffuse solar irradiance on inclined surface $\left[\frac{\text{W}}{\text{m}^2}\right]$	V_{MP}	voltage at maximum power point
		V_{OC}	voltage at open circuit condition

sources of data: punctual measurements collected on the ground by weather stations and maps generated by devices installed on satellites. Ground mounted weather stations are sparsely distributed all over the world and measure the solar irradiation at ground level in a given location with different time resolutions (i.e. 10 min to 3 h or greater). Since the cost of the installation and maintenance of a ground based network are significant, the density and coverage in each country vary. On the other hand, devices installed on satellites can permanently scan the Earth's surface from different perspectives. Satellites record images of the earth at different wavelengths. These data are then used to estimate the cloud cover and the corresponding solar irradiation at ground level [4–6].

Both methods and technologies have advantages and downsides, leading to errors depending on the location and the boundary climate conditions, and for these reasons have been investigated in previous work in order to identify their main differences. Concerning the usage of ground-based measurements, researchers have recently evaluated and assessed interpolation methods using different time resolution, latitudes and elevations to identify the impact of different boundary conditions on the results.

First studies aiming at the generation of continuous maps of the solar radiation from ground-station measurements used different techniques such as spline functions, weighted average procedures or kriging [7–9]. The widely used r.sun [10] method is implemented in GRASS GIS and designed based on the equation of ESRA (European Solar Radiation Atlas) [11,12], which provided a significant contribution in terms of accuracy and progress compared to previous models. GIS-based models were implemented to estimate the spatial distribution of the solar radiation with monthly and daily temporal resolution in South Korea [13], Fujian Province with an annual temporal resolution [14], and Auckland, New Zealand [15] using ESRI's solar radiation analyst.

Unlike methods used at ground stations, satellite data and maps have the advantage to provide a large spatial and temporal resolution. In [16], the uncertainties when combining ground based measurements and satellite images are investigated. Five models converting satellite images into different radiation components (i.e. global and beam irradiance) were validated in [17] using the measurements collected in

2006 from 23 ground stations located in Europe at latitudes between 20° and 60°. The study shows that the global horizontal irradiance is retrieved with a mean bias of 1% (i.e. $4 \frac{\text{W}}{\text{m}^2}$) and that an average standard deviation of 16% (i.e. $55 \frac{\text{W}}{\text{m}^2}$) is achieved by the algorithm with best performance. The uncertainty of the generated maps was assessed using ground measurements from 27 meteorological stations available in Spain.

Previous work therefore demonstrated that satellite images of the solar radiation provide data in the form of continuous maps with different spatio-temporal resolution which must be validated (or complemented) using ground based measurements to quantify their accuracy. Nevertheless, despite these uncertainties, satellite or interpolated maps of the solar radiations are often used to determine the PV electricity generation with different time resolution and in different regions of the world such as Hong Kong [18], Greece [19], Piedmont [20] and the Canary Islands [21]. Despite differences in spatio-temporal resolution, satellite-derived data offer the unquestionable advantage to cover large areas and time periods, which is more reliable than extrapolating point measurements of ground based weather stations using statistical or geometrical approaches. For these reasons, satellite data offer a practical advantage when assessing the PV potential over large regions.

As aforementioned, the estimate of the PV potential on rooftops over large regions has multiple advantages and various approaches have been proposed combining GIS data and climate data. In order to quantify the PV potential over large regions, empirical methods were used to combine satellite images, building footprints and statistical data to quantify the available rooftop areas. The disadvantage of these methods concerns the large uncertainties when estimating the rooftop surfaces and thus the PV potential. Recent studies demonstrated that the use of LiDAR data significantly improves the identification of rooftop geometries [22–25,15] and thus estimate the PV electricity generation with a higher accuracy, the PV electricity generation [26–29]. Although these data allow for a significant increase in accuracy, one of the disadvantages of LiDAR data is the lack of large-scale availability. An alternative to LIDAR data are 3D city models [30–32].

However, as they are often derived from LIDAR data, they are typically available in fewer areas.

With the development and application of PV technology for electricity generation, an accurate prediction of the solar radiation, at a fine time scale (i.e. 10 min to annual resolution) is critical and fundamental in order to estimate the PV contribution to the energy demand and to assess its impact on the power grid [33,34]. Since the contribution of PV technology to the energy supply is becoming more and more significant, it is also fundamental to accurately model both the spatio-temporal distribution of the solar radiation as well as the estimates of the energy production. This is an important aspect because the electricity generation is the effective energy output fed into the power grid and thus counted as part of the contribution to the energy supply. Such improvements result in significant advantages in multiple fields spanning from the controlling and management of distribution grids [35–37], electric vehicles [38], building heat demand [39] to the setting of energy policies [40,24]. In order to achieve such goals, the validation of these models and data is necessary in order to quantify their accuracy.

For the aforementioned reasons, the contributions of this work are twofold: first, we present a scalable method to estimate the PV irradiation potential and electricity production on building rooftops over large regions using satellite based solar irradiation data. We consider a study area which is considerably larger compared to previous work. In comparison to [41], which is among the studies with the largest spatial coverage, a study area of 2250 km² is considered with a spatial resolution of 1 m². We applied our method to a study area of 41,285 km² and a spatial resolution of 0.5 m². By simulating over 3 million buildings we demonstrate the scalability and applicability of our method to simulate large regions. This is the first study that simulates the solar potential for a whole country with a bottom-up model. Second, we apply this method to estimate and compare the electricity production of 500 PV plants located in Switzerland using GIS. By doing this, we can estimate the accuracy of the model for predicting the electricity production using different PV technologies. The model does not only calculate monthly long-term mean estimates, but also considers the monthly variability between different years. This is an important aspect for the integration of PV into the power grid, which has been neglected previously. Furthermore, this is the first study, available in the literature to our knowledge, where such a large validation has been carried out. The model couples satellite images of the solar radiation with the technical specifications of PV components provided by the manufacturers. The developed generic method is applied to Switzerland but can be used in any region for which the datasets mentioned in the next section are available. An additional interesting aspect is the selection of the studied region which made this study particularly challenging. Switzerland is a country characterized by complex topography, which impacts the distribution of the shadows over the year and the formation of clouds, therefore making the modelling more complex. The results of the validation process provide an overview of the spatial distribution of the uncertainties of the model used for electricity generation.

The second section will present the data used in the model applied to estimate the electricity generation which is introduced in the third section. In the fourth section, the results of the spatial distribution of the solar radiation and the validation process are introduced and, finally, discussed in the last section.

2. Data

2.1. Building footprints

The building footprints used in this study comes from three different sources: cadastral survey, Open Street Map (OSM) and SwissTLM. We utilize three different sources because the official cadastral survey does not cover Switzerland entirely, although it provides the most accurate (and official) dataset. We filled in the gaps of the missing buildings in

the cadastral survey using the datasets from OSM and SwissTLM3D.¹ SwissTLM3D is the official topographical landscape model of Switzerland providing also the polygons of the building footprints. The combined dataset contains 88.91% of the building footprints from the cadastral survey, 6.86% from OSM and 4.22% from SwissTLM3D.

The quality and accuracy of the building footprints vary between the different datasets. As the position accuracy of the cadastral survey is required to be less than 10 cm [42] it is the most accurate dataset. The quality of the OSM building footprints, due to their nature as user generated content, can vary between different regions both regarding accuracy and completeness. A study analyzed the accuracy of OSM buildings for the city of Munich [43]. It was found that OSM buildings are almost identical in shape to a reference dataset of the cadastral survey, however, an offset was present due to the aerial imagery used to digitize the building footprints.

The total area of the building footprints used in this study is 48,536 ha. In comparison, in the latest land use statistics of 2009, the Swiss Federal Statistical Office declares a building area of 50,540 ha [44]. This difference of 4% can be explained by the different survey method (aerial imagery) of the land use statistics.

2.2. Digital elevation models

Digital elevation models (DEM) represent the topographic surface of the terrain. One distinguishes between digital surface models (DSM), representing the surface including all objects above ground – such as canopies of vegetation or buildings – and digital terrain models (DTM) representing the elevation of the bare ground. In DSM or DTM the elevation is represented as a regularly spaced grid (also referred to as raster). Each cell of the grid has an assigned elevation value.

The Swiss Federal Office of Topography (swisstopo) provides both the DSM and DTM raster datasets with a spatial resolution of two meters for all of Switzerland. Both datasets are derived from the same LIDAR (Light Detection and Ranging) point cloud. This cloud was created between 2001 and 2008 and has as a low point density of approximately $1 \frac{\text{Point}}{\text{m}^2}$. Due to the applied smoothing and the low spatial resolution, the DSM provided by Swisstopo does not represent buildings accurately. In Buffat [22], a method was developed to improve the interpolation of building rooftops for low density point clouds using building footprints.

Both the swisstopo DSM as well as the newly interpolated DSM were compared with a reference DSM using over 70,000 buildings of the city of Zurich. In contrast to the swisstopo DSM, the reference DSM has a spatial resolution of 0.5 m and was derived from a point cloud of $8 \frac{\text{Points}}{\text{m}^2}$. The interpolated DSM from the low density points cloud showed a comparable accuracy to the reference DSM. However, while planar parts of roofs are smoothly interpolated, small features such as chimneys are lost due to the small point density. This is due to the low number of data points that cannot be differentiated from outliers.

In this work we used multiple DSM of Switzerland with a resolution of 0.5 m. We applied the method of Buffat [22] to the whole LIDAR point cloud. However, due to the age of the swisstopo LIDAR point cloud, we utilized more recent DSM where possible. This is the case for the cantons of Zurich, Bern, Jura, Aargau, Schaffhausen, Zug, Glarus, Solothurn, Neuchâtel, Geneva, and Basel-Landschaft.

2.3. Solar irradiation

The Satellite Application Facility on Climate Monitoring (CM SAF) Surface Solar Radiation Data Set – Heliosat (SARAH) [45] provides solar irradiance data which covers the area of $\pm 65^\circ$ longitude and $\pm 65^\circ$ latitude with a spatial resolution of 0.05° . For Switzerland, this results in a resolution of roughly 3.8 km for the longitude and 5.6 km for the

¹ <https://shop.swisstopo.admin.ch/en/products/landscape/tlm3D>.

latitude. The dataset provides time series from 1983 to 2015 with a temporal resolution of up to 30 min. However, for this work we only used the data from 1993 to 2015 as only this time period was available to us in a 30 min resolution. For each day and time step, the datasets provide global irradiance (the total irradiance on a flat surface), the direct normal irradiance (the direct beam component of the global irradiance normalized with the cosine of the solar zenith angle) as well as the cloud albedo. In [46], the CM SAF dataset was validated against the measured data of 104 weather stations of Switzerland provided by the Federal Office of Meteorology. The validation showed a mean bias of $0.18 \pm 8.54 \left[\frac{\text{W}}{\text{m}^2} \right]$ for stations below 1000-m elevation. For higher elevations, the dataset underestimates the solar irradiance. Around 87% of all buildings in Switzerland are below 1000 m [46].

3. Methods

The solar irradiation on a rooftop depends on various spatial and temporal properties, such as the position of the sun or the obstruction of the direct path to the sun. The computational complexity renders it infeasible to calculate the solar irradiation for each rooftop and half-an hour interval of the solar irradiation dataset on a single computer. To be able to process large regions, the method presented here is designed to be parallelizable. In the first part of this section, we discuss the model used to estimate the solar irradiation potential on building rooftops. The solar irradiation potential corresponds to the amount of irradiation that reaches a rooftop. While the solar irradiation potential is independent of technology, the actual electricity production of a PV system depends on the selected technology. The second part of this section discusses the model to derive monthly electricity production. It is used to validate our approach against actual measured electricity production of PV systems installed in Switzerland.

3.1. Solar irradiation potential on building rooftops

The process to estimate the solar irradiation potential on building rooftops is divided into the three phases shown in Fig. 1. In the first phase,

for each cell of the solar irradiance dataset presented in Section 2.3 monthly irradiance profiles with a half-hour time resolution are calculated. Thereby three scenarios are considered: long-term mean, monthly first quartile and monthly third quartile. Details of the process can be found in Section 3.1.1. In the second phase, intermediate datasets for orientations, slope and horizon angles are computed for each building. This phase is described in Section 3.1.2. The estimation of the solar irradiation on rooftops, the final third phase, is discussed in Section 3.1.3.

3.1.1. Monthly solar irradiance profiles

The goal of this phase is the creation of monthly solar irradiance profiles on inclined surfaces for each month and cell of the solar radiation dataset. These profiles are precomputed for inclined surface with different orientations (α) and slope (β). The precomputed inclined irradiances can then be used for all buildings located within the same cell of the solar dataset. Thus these precomputed profiles serve as lookup tables later when the rooftop irradiation potential is estimated for each building. For each cell and half hour, the solar radiation satellite dataset contains the diffuse (G_D) and direct beam irradiance (G_B) on a horizontal plane in $\frac{\text{W}}{\text{m}^2}$. The global irradiance on a horizontal plane (G_G) can be calculated by adding G_B and G_D . Both orientation and slope of an inclined surface influence the solar irradiance. Thus, the irradiance for orientations from -180 to 180 in 15 degrees steps and for slopes from 0° to 90° in 10 degree steps are calculated for direct, diffuse and reflected radiation using Eqs. (1)–(3).

$$G_{B,\alpha,\beta} = \frac{G_B}{\cos\theta_z} * \cos\theta_i \quad (1)$$

In Eq. (1), the direct solar irradiance on an inclined surface ($G_{B,\alpha,\beta}$) is geometrically calculated from the direct horizontal solar irradiance (G_B) using the solar zenith angle (θ_z) as well as the incidence angle on an inclined surface (θ_i) as in Duffie [47, p. 24]. The angles θ_i and θ_z are calculated using the solar position algorithm (SPA) of the National Renewable Energy Laboratory (NREL) [48]. Both θ_i and θ_z depend on the location of the observer. For the solar irradiation dataset, the centroid of each cell was used as the location.

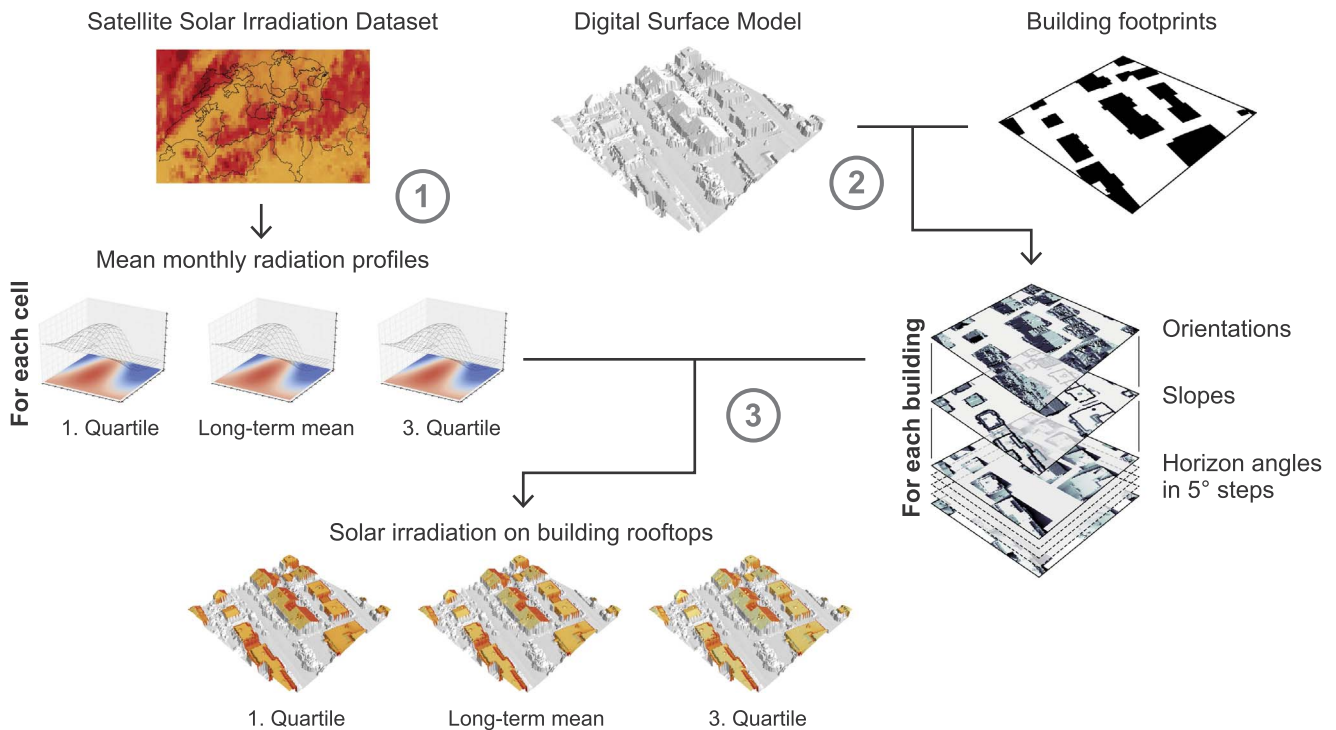


Fig. 1. Workflow 1. derivation of mean monthly irradiance profiles for solar irradiance datasets; 2. computation of intermediate datasets; 3. estimation of the solar irradiation potential on rooftops.

$$G_{D,\alpha,\beta} = G_D \left[F_1 \frac{a}{b} + (1-F_1) \frac{1 + \cos\beta}{2} + F_2 \sin\beta \right] \quad (2)$$

Various models derive the diffuse irradiance ($G_{D,\alpha,\beta}$) on inclined surfaces [49]. We selected the model of Perez since previous studies demonstrated that it performs well under different sky conditions [50,51]. The diffuse solar irradiance on an inclined surface is computed using Perez's model [52] with Eq. (2), whereby $a = \max(0, \cos\theta)$, $b = \max(\cos 85^\circ, \cos\theta_z)$ and both F_1 and F_2 are empirical constants [52].

The reflected solar irradiance ($G_{R,\alpha,\beta}$) is calculated using Eq. (3) from [50] with a constant albedo of $\rho = 0.2$.

$$G_{R,\alpha,\beta} = \rho * G_G * \frac{(1 - \cos\beta)}{2} \quad (3)$$

Finally, the global solar irradiance on an inclined surface ($G_{\alpha,\beta}$) is calculated using Eq. (4).

$$G_{\alpha,\beta} = G_{B,\alpha,\beta} + G_{D,\alpha,\beta} + G_{R,\alpha,\beta} \quad (4)$$

For each of the available 375,136 half-hour records from 1993 to 2015 and 4559 cells of the solar irradiance dataset covering Switzerland, as well as the above mentioned 216 combinations of α and β , the irradiance values on inclined surfaces ($G_{\alpha,\beta}$) are computed. Then for each month, long-term mean profiles are aggregated by averaging all values within the same month, orientation and slope. Fig. 2 shows the long-term mean irradiances of one cell for the August monthly profile at 13:30. Each of these half-hour time steps are then interpolated with a 1-degree step size for both slope and orientation using bivariate spline interpolation with a degree of 3.

The profiles for the first and third quartile scenarios are computed similarly. Instead of aggregating mean profiles over the whole period, mean monthly profiles are aggregated for all individual years of the solar irradiation dataset excluding years with incomplete recordings. The monthly averages of all years are then ranked as a function of the mean monthly solar irradiation. For each cell and month, the profile of the year with the first and third quartile rank are used for the first, respective third quartile scenario.

3.1.2. Horizon angles, slope and aspects

Surfaces are shaded if the direct path of the light from the sun is obstructed. This happens when the elevation angle of the sun (θ_H) is smaller than the horizon angle (θ_{Hor}) of the local horizon of the observer (Fig. 3).

To reduce computational effort, horizon angles for different orientations are calculated with two methods. The first method uses the 0.5 m DSM with a buffer zone of 500 m around each building (θ_{Hor1}). For each cell of the DSM of a building, horizon angles of the surrounding topography are computed by varying the orientation with a step size of 5° . The second method computes the horizon angles from the midpoint of the building using the lower two-meter resolution DEM for the same orientation angles with a large sample distance of 5000 m (θ_{Hor2}). While the first method takes small local features such as neighbouring objects into account, the second method allows modelling the effect of hills or mountains. For the final horizon angle (θ_{Hor}), the maxima of the horizon angles of both methods are used for each cell and orientation.

In addition to the horizon angles for different orientations, slope (β) and aspect (α) are computed using the DSM.

3.1.3. Solar irradiation on rooftops

In the third and last phase the solar irradiation on rooftops is estimated. For each cell of a building dataset we retrieve its orientation (α) and slope (β) from the pre-processed datasets of phase two. For each half hour of a typical day the orientation (α_S) and elevation angle (θ_z) of the sun are calculated using the solar position algorithm (SPA). The horizon angle of the sun is then derived using Eq. (5).

$$\theta_H = 90^\circ - \theta_z \quad (5)$$

For each time step, it is detected whether the sun is below the horizon ($\theta_H \leq \theta_{Hor}$) and thus the cell is shaded. In this case only diffuse irradiance and no direct irradiance reaches a cell (see Eq. (6)). This is achieved by looking up the horizon angle closest to the orientation of the sun α_S in the precomputed horizon angles of phase two.

$$G_{\alpha,\beta,t} = \begin{cases} G_{D,\alpha,\beta,t} + G_{R,\alpha,\beta,t} & \theta_H \leq \theta_{Hor} \\ G_{B,\alpha,\beta,t} + G_{D,\alpha,\beta,t} + G_{R,\alpha,\beta,t} & \theta_H > \theta_{Hor} \end{cases} \quad (6)$$

The irradiation I_m for each month (m) is then calculated by aggregating the half-hour time steps (t) of each monthly profile using Eq. (7). This calculation is performed for each cell of the building datasets.

$$I_m = \sum_{t=1}^{48} \frac{1}{2} * \text{days of month} * G_{\alpha,\beta,t} \quad (7)$$

3.2. PV system model

The conversion of solar radiation to electricity depends on the technical components and characteristics of the PV system. The characteristics of components when converting solar radiation into electricity are shown in Fig. 4. First, the performance of PV panels (η_{module}) is a function of radiation (G), temperature (T) and properties of the selected panel. The efficiency of the inverter (η_{inv}) depends on the selected unit and inlet power (P_{DC}). Furthermore, the model includes the losses of the internal network, soiling and degradation due to age.

3.2.1. PV module efficiency

Solar radiation is transformed into electricity with photovoltaic (PV) modules. In recent years, many studies developed models for PV systems based on electrical equivalent circuits, such as single diode [53] or double diode models. Thereby the double diode variant is known to better model the behaviour of PV cells at low illuminations compared to the single diode model [54]. Comprehensive reviews of such models can be found in [55,56]. These models aim at assessing the efficiency and performance under various operating conditions, and vary by computational complexity and amount of required input data. The challenge is that the necessary parameters of the electrical equivalent circuits are commonly not directly available from the datasheet of the modules. For this study, the single-diode electrical equivalent based model of Batzelis [57] is used. Its advantage is that it allows for estimating all required input parameters from datasheet values with explicit equations, avoiding the requirement to solve a nonlinear equation system such as in [53]. The required input parameters include:

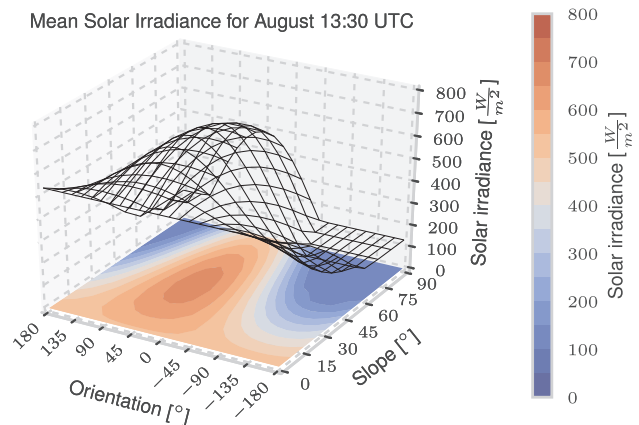


Fig. 2. Example of precomputed irradiance levels for different slopes and orientations of the typically monthly long-term mean profile for August 13:30 for one cell of the solar irradiation dataset.

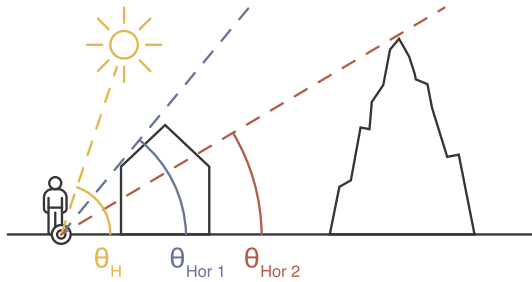


Fig. 3. Illustration of horizon angle θ_{hor1} and (θ_{hor2}) .

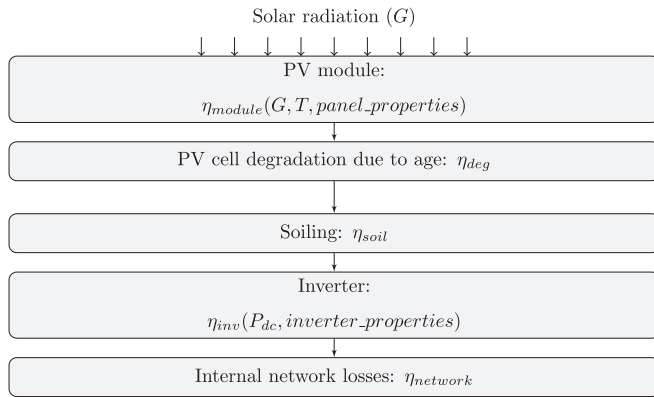


Fig. 4. PV system model takes into account the efficiency of the solar cells depending on solar irradiance (G), temperature (T) and cell properties, degradation of the PV cells due to age, soiling, inverter efficiency, and other losses.

- the number of cells in parallel (N_p),
- the number of cells in series (N_s),
- the voltage at open circuit condition (V_{OC0}),
- the current at short-circuit condition (I_{SC0}),
- the voltage and current at maximum power point condition (V_{MP0} , respectively I_{MP0}),
- the temperature coefficient of short circuit current (α_{ISC}) and open circuit voltage (β_{VOC}),
- as well as the nominal operating cell temperature (T_{ref}).

Nominal Operating Cell Temperature (NOCT) conditions are under an air temperature of 20 °C and an irradiance of $800 \frac{W}{m^2}$. Furthermore, the area of one cell of the panel as well as the total panel area are required to derive the panel efficiency. Using these parameters, Batzeli' model [57] estimates the five parameters of the single diode model at NOCT conditions: modified diode ideality factor (a_0), photo-current (I_{ph0}), diode saturation current (I_{s0}), series resistance (R_{s0}) and shunt resistance (R_{sh0}) using Eqs. (8)–(14). $W()$ stands for the Lambert function.

$$\delta_0 = \frac{1 - 298.15 * \beta_{VOC}}{50.1 - 298.15 * \alpha_{ISC}} \quad (8)$$

$$w_0 = W\left(e^{\frac{1}{\delta_0} + 1}\right) \quad (9)$$

$$a_0 = \delta_0 * V_{OC0} \quad (10)$$

$$R_{s0} = \frac{a_0 * (w_0 - 1) - V_{MP0}}{I_{MP0}} \quad (11)$$

$$R_{sh0} = \frac{a_0 * (w_0 - 1)}{I_{SC0} * \left(1 - \frac{1}{w_0}\right) - I_{MP0}} \quad (12)$$

$$I_{ph0} = \left(1 + \frac{R_{s0}}{R_{sh0}}\right) * I_{SC0} \quad (13)$$

$$I_{s0} = I_{ph0} * e^{\frac{-1}{\delta_0}} \quad (14)$$

Based on Eqs. (15)–(21) the five parameters of the single diode model are adjusted for non-standard conditions for cell temperature (T) and irradiance level (G) based on equations from [53,58]. Thereby the irradiance at standard test conditions (G_{ref}) is $1000 \frac{W}{m^2}$, k the Boltzmann constant and q the elementary charge.

$$a = a_0 \frac{T}{T_{ref}} \quad (15)$$

$$E_g = 1.16 - 7.02 * 10^{-4} * \left(\frac{T^2}{T - 1108}\right) * q \quad (16)$$

$$E_{g,ref} = 1.16 - 7.02 * 10^{-4} * \left(\frac{T_{ref}^2}{T_{ref} - 1108}\right) * q \quad (17)$$

$$I_s = I_{s0} * \left(\frac{T}{T_{ref}}\right)^3 * \exp\left(\frac{E_{g,ref}}{k * T_{ref}} - \frac{E_g}{k * T}\right) \quad (18)$$

$$I_{ph} = \frac{G}{G_{ref}} * (I_{ph0} + \alpha_{ISC} * (T - T_{ref})) \quad (19)$$

$$R_{sh} = \frac{G_{ref}}{G} * R_{sh0} \quad (20)$$

$$R_s = R_{s0} \quad (21)$$

Using the adjusted parameters a, I_s, I_{ph}, R_{sh} and R_s the current (I_{MP}) and voltage (V_{MP}) at the maximum point are computed using Eqs. (22)–(24) developed by Batzeli [59]. The current at short circuit condition (I_{SC}) is calculated by setting the voltage (V) in Eq. (25) to 0.

$$w = W\left(\frac{I_{ph} * e}{I_s}\right) \quad (22)$$

$$V_{MP} = \frac{R_s + R_{sh}}{R_{sh}} * a * (w - 1) - R_s * I_{ph} * \left(1 - \frac{1}{w}\right) \quad (23)$$

$$I_{MP} = I_{ph} * \left(1 - \frac{1}{w}\right) - a * \frac{w - 1}{R_{sh}} \quad (24)$$

The voltage in open circuit condition (V_{OC}) is defined as the voltage when the current (I) is 0. It is determined by bisection of Eq. (25) in the interval $V = 0$ to $V = 2 * V_{OC}$. I_{SC} is calculated by setting V to zero in Eq. (25).

$$I = \frac{R_{sh} * (I_{ph} + I_s) + R_{sh} * V}{(R_s + R_{sh})} - \frac{a}{R_s} * W\left(\frac{e^{\frac{R_s * R_{sh} * (I_{ph} + I_s) - V}{a * (R_s + R_{sh})}}}{\frac{a * (R_s + R_{sh})}{(R_s * R_{sh} * I_s)}}\right) \quad (25)$$

The efficiency of a solar cell (η_{cell}) is determined using Eqs. (26) and (27) [60]. First, using V_{MP}, I_{MP}, V_{OC} and I_{SC} the fill factor (FF) is calculated with Eq. (26). Then, with Eq. (27) the efficiency of a cell is calculated by dividing the maximum potential power production of the cell by the current level of solar radiation (G).

$$FF = \frac{V_{MP} * I_{MP}}{V_{OC} * I_{SC}} \quad (26)$$

$$\eta_{cell} = \frac{V_{OC} * I_{SC} * FF}{G} \quad (27)$$

A PV module typically consists of a series of cells that are in series (N_s), or are in parallel (N_p). The total number of cells per panel (N) equals $N_s * N_p$. Typically, not the complete area of a PV module (A_{panel}) is covered by cells. The remaining area is not able to produce electricity and is considered in Eq. (28) to determine the efficiency of the PV module.

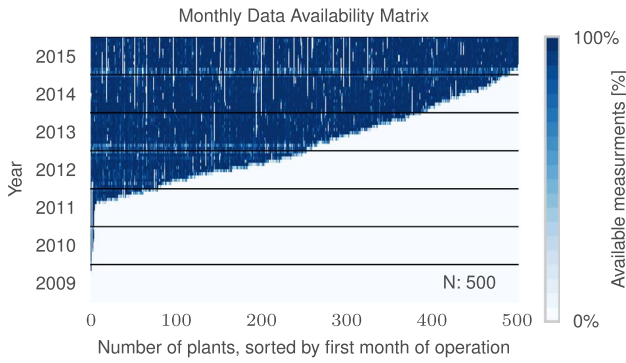


Fig. 5. Completeness of monthly measurements by plant.

$$\eta_{\text{module}} = \eta_{\text{cell}} * \frac{A_{\text{cell}} * N}{A_{\text{panel}}} \quad (28)$$

3.2.2. Degradation

PV cells are susceptible to degradation over time. Based on [3] a yearly degeneration rate (r) of 0.9% is assumed and calculated using Eq. (29).

$$\eta_{\text{deg}} = (1-r)^{\frac{\text{age in months}}{12}} \quad (29)$$

3.2.3. Inverter efficiency

The inverter efficiency is calculated using the PVWATT model [61]. This model is based on fitting a quadratic loss model to inverter performance data from the California Energy Commission (CEC). The estimated efficiency curve is then scaled (using ζ) to an actual inverter using its nameplate specifications. Thus, the model requires the direct current (DC) input (P_{dc}), the nameplate DC rating (P_{dc0}) as well as the nominal inverter efficiency (η_{nom}) as input. As reference inverter efficiency (η_{ref}) a typical value of 0.9637 is used, which is based on the CEC data [61]. The alternative current (AC) nameplate rating (P_{ac0}) is thereby determined using Eq. (31). Using Eqs. (30)–(33) the output AC current depending on the input DC current and the inverter nameplate rating are calculated. For our analysis we used the PVLIB-Python implementation of the model [62].

$$\zeta = \frac{P_{\text{dc}}}{P_{\text{dc0}}} \quad (30)$$

$$P_{\text{ac0}} = P_{\text{dc0}} * \eta_{\text{nom}} \quad (31)$$

$$\eta_{\text{inv}} = \frac{\eta_{\text{nom}}}{\eta_{\text{ref}}} \left(-0.0162 * \zeta - \frac{0.0059}{\zeta} + 0.9858 \right) \quad (32)$$

$$P_{\text{ac}} = \begin{cases} \eta_{\text{inv}} * P_{\text{dc}} & 0 < P_{\text{dc}} < P_{\text{dc0}} \\ P_{\text{ac0}} & P_{\text{dc}} \geq P_{\text{dc0}} \\ 0 & P_{\text{dc}} = 0 \end{cases} \quad (33)$$

3.2.4. Other losses

Based on [63], 5.86% losses are assumed for soiling (η_{soil}) and 2% for internal network losses (η_{network}).

4. Results and validation

In order to validate the proposed models, we used a dataset of measured electricity production of multiple PV plants located in Switzerland. The dataset consists of publicly available data of the solarlog-web portal² which allows users to visualize and publicly share

data of their PV installations. This dataset includes, for each PV plant the electricity production measured at the inverters with a time resolution of five minutes, the zip area code of the plant and information about PV panels and inverters. For each type of installed PV panel, the following pieces of information are provided: slope, orientation, number of panels of the same type, name of the manufacturer and name of the model. For inverters, the number of the same type, the name of the manufacturer and the model type are specified. The complete dataset contains 1883 PV plants across all of Switzerland, thereby only the 1099 plants having a commissioning date before 2015 (and thus providing at least 12 months of validation data) are used.

The matching of PV modules to datasheet values was done manually. Only around 50% of the processed plants could be matched to datasheet values due to ambiguous descriptions. Further exclusion reasons are plants that were modified over their lifetime, the indication of slopes or orientations was ambiguous, or the plant had a maximum monthly capacity factor of over 40%. Such high capacity factors are unrealistic for Switzerland [64]. Only one plant had such a high value. In the end, 500 plants were used for the validation.

It is worthwhile to mention that the electricity production is measured by data logger devices and automatically submitted to the portal while all other data for each plant are user generated. An analysis of the data revealed that the time series of electricity generations are not always complete. This can be due to technical errors of the PV systems, failure of data transmission or other errors. Since missing records influence the results of the validation process, we developed the following methodology in order to measure the completeness of the data set. For each day, we calculated the percentage of measurements with an electricity production greater than zero during the period of the day when the sun's elevation is greater than 10° over the horizon. Then for each month, the mean percentage of all days is calculated. Fig. 5 shows the resulting monthly data availability matrix. The monthly availability is indicated by blue³ color. Bright colors refer to months with no or only a few available measurements, dark blue colors indicate complete recordings for this month. In the period of winter 2012/2013 and 2014/2015, a pattern of poor data availability through nearly all of the PV plants can be observed.

Fig. 6a shows the count of PV plants for different sizes of installed capacity as well as PV panel technologies. In total, 365 plants use panels of mono, 96 poly and 39 thin film technology. As seen in Fig. 6b most of the PV panels are installed on flat or inclined building roofs with slope angles below 15° and 50°. Panels with a slope smaller than 15° are most likely mounted on flat roofs using racks with a small slope. Only 5 panels have a slope greater than 55° and only two of them have a slope of 90° and are thus most likely mounted on a wall.

Since the external temperature influences the efficiency and performance of the PV systems, we need time series of the temperature profiles in Switzerland with the same temporal resolution as the time series of the solar radiation. For the 46 weather stations shown in Fig. 7, complete hourly temperature readings measured 2 m above ground are available for the period from 2009 to 2016. For each day and station, a half-hour time series of the temperature is interpolated from the hourly values. For each PV plant location, the data of the nearest weather station are used. Fig. 7 shows the spatial distribution of the stations.

Matching the names of all inverters to the datasheet with technical specifications of the inverters provided by the manufacturers was not always possible due to the lack of detailed model names in the metadata of the PV plants. For plants without inverter information, an inverter with an efficiency of $\eta_{\text{nom}} = 95\%$ and rated power of P_{dc0} of the maximum of the measured input power was set. In the case when plants have multiple inverters, each inverter is assigned a share of the electricity production proportional to its rated power.

³ For interpretation of color in 'Figs. 5 and 8', the reader is referred to the web version of this article.

² <http://home.solarlog-web.ch/switzerland.html>.

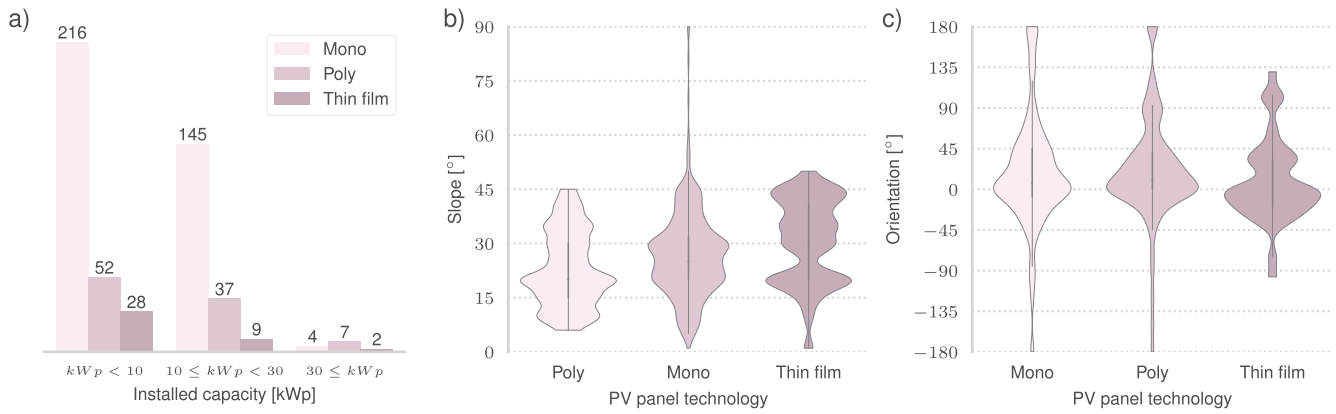


Fig. 6. (a) Number of PV plants depending on installed capacity and PV technology. (b) Distribution of slopes in the validation dataset. (c) Distribution of orientations (c) in the validation dataset. Violin plots are similar to boxplots, but show instead of the box and the whisker the kernel density estimation on both sides of the axis.

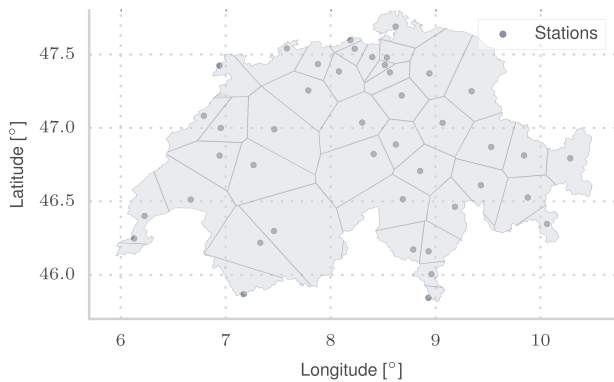


Fig. 7. Weather stations measuring temperature (dots) and their areas of use (areas).

Using the presented models the monthly electricity production is estimated for each of the validation plants. All months having not at least 95% of all recordings are excluded from the validation. This results in a total of 11,817 months. Fig. 8 shows a comparison of measured and modelled electricity production. Due to the large number of data points, we use hexagonal cells instead of individual data points for visualisation. The color of each hexagonal cell is determined by the number of data points of the cell using a logarithmic scale. With a goodness of fit (R^2) of 0.97, the model demonstrated a very good fit

regardless of the plant size. However, due to different sizes of the PV plants in the validation dataset the majority of monthly productions are less than 5 MWh. Fig. 8 shows the comparison of capacity factors derived from the recorded and modelled production. In contrast to the produced energy, the capacity factor is a unitless figure. It is defined as the ratio of the actual energy production over a given period to the maximum possible technical electricity production based on the installed capacity. Through its normalizing character the capacity factor is more suitable to compare plants of different sizes of installed capacity. With R^2 of 0.90 the model again shows a very good correlation with the measured recordings, although a slight overestimation can be detected for capacity factors below 10%.

Fig. 9 shows boxplots of the relative errors for each month and PV technology. The plot demonstrates that the model performs well for the majority of the months, in particular, when the solar irradiation is stronger and contributes most to the annual electricity generation. In addition, in these months, the model performs equally well for all technologies. The installed PV technologies are mono-crystalline (mono), poly-crystalline (poly) and heterojunction with thin film layer (thin film). Results show that the model overestimates the electricity production in the period from November to January. Due to a lower solar irradiation, these months do not heavily influence the yearly estimates. Fig. 10 shows the spatial distribution of the goodness of fit for the plants used for the validation. The shown coordinates of the plants corresponds thereby to the centroid coordinates of the zip code area

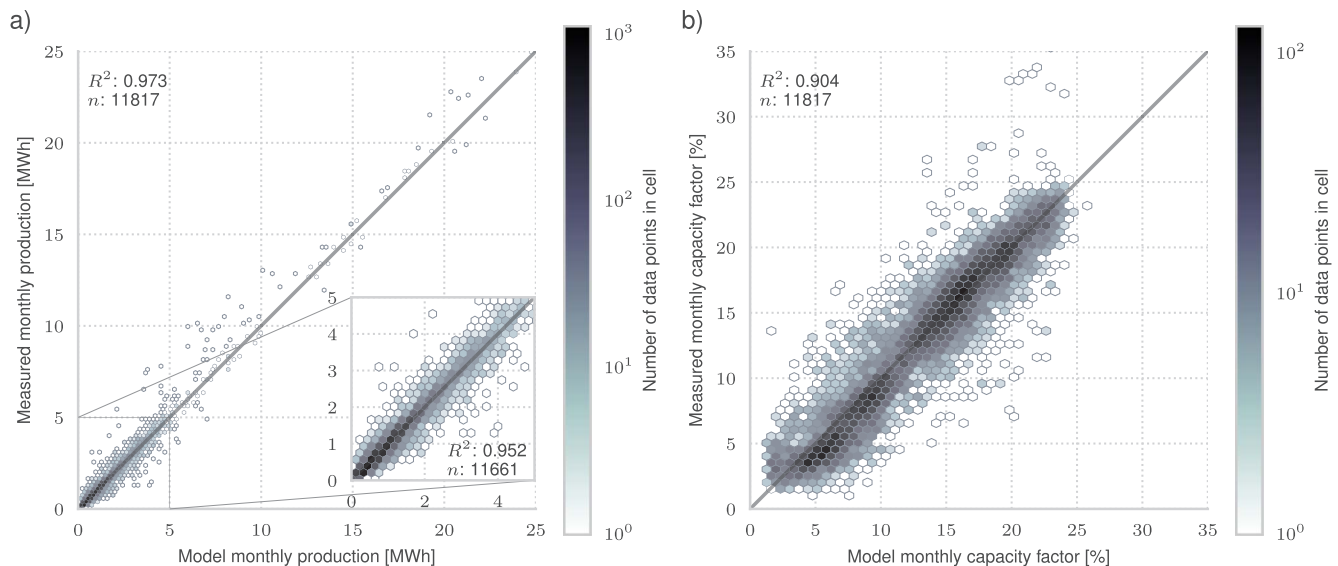


Fig. 8. (a) Comparison of measured and modelled electricity production. (b) Comparison of monthly capacity factors of modelled and measured electricity production.

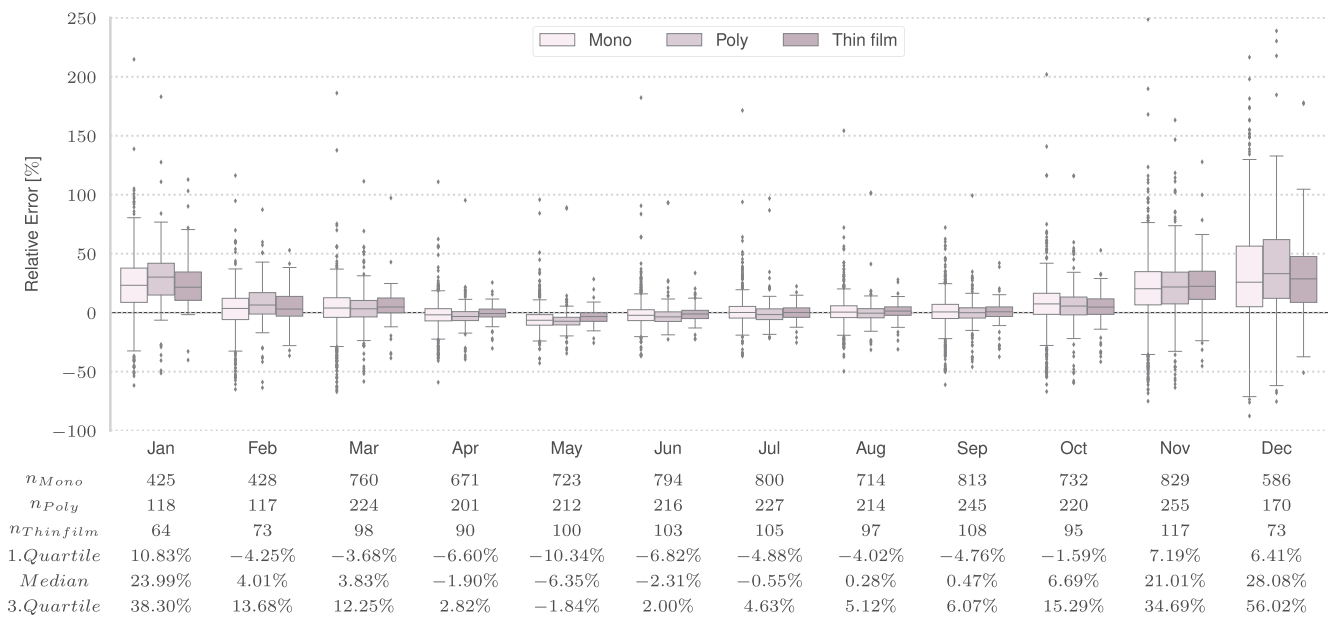


Fig. 9. Boxplot of relative errors for different months and PV technologies. The size of the whiskers of the boxplots corresponds to 1.5 times of the interquartile range (IQR). The table below the plots indicates the number of samples per category. One outlier in January and six outliers in December with a maximal relative error of 657% were omitted to improve readability.

they are located in. Most of the plants are located in the northern part of Switzerland, whereas only a few plants are located in the Alps and the South. Compared to the rest of Switzerland in these regions a higher share of plants have a worse fit.

Using the solar radiation model presented in Section 3.1, the long-term mean, 1st quartile and 3rd quartile values of the solar radiation potential are estimated for Switzerland using all available buildings. The total rooftop area is 48,536 ha on which the yearly solar irradiation is 470 TW h, 514 TW h respectively 568 TW h corresponding to the 1st quartile, long-term mean and 3rd quartile values. With an assumed capacity factor of 10.33% (see Appendix A) this would result in an

annual potential electricity production of 48.6, 53.2 respectively 58.8 TW h for the three scenarios. In contrast, the total Swiss electricity consumption in 2015 was 58.3 TW h [65]. As the solar irradiation has a large seasonal discrepancy between summer and winter, it can not be concluded that the solar potential can cover the Swiss electricity demand for a typical year. Only a small amount of rooftop area has a mean yearly irradiation greater than $1400 \frac{\text{kWh}}{\text{m}^2 \cdot \text{year}}$. This is due to the fact that the highest yearly solar irradiation is available in the mountainous regions with high elevation where only a few buildings are located.

For policy makers the mean yearly irradiation is an important indicative value to be used in order to derive the economic feasibility of

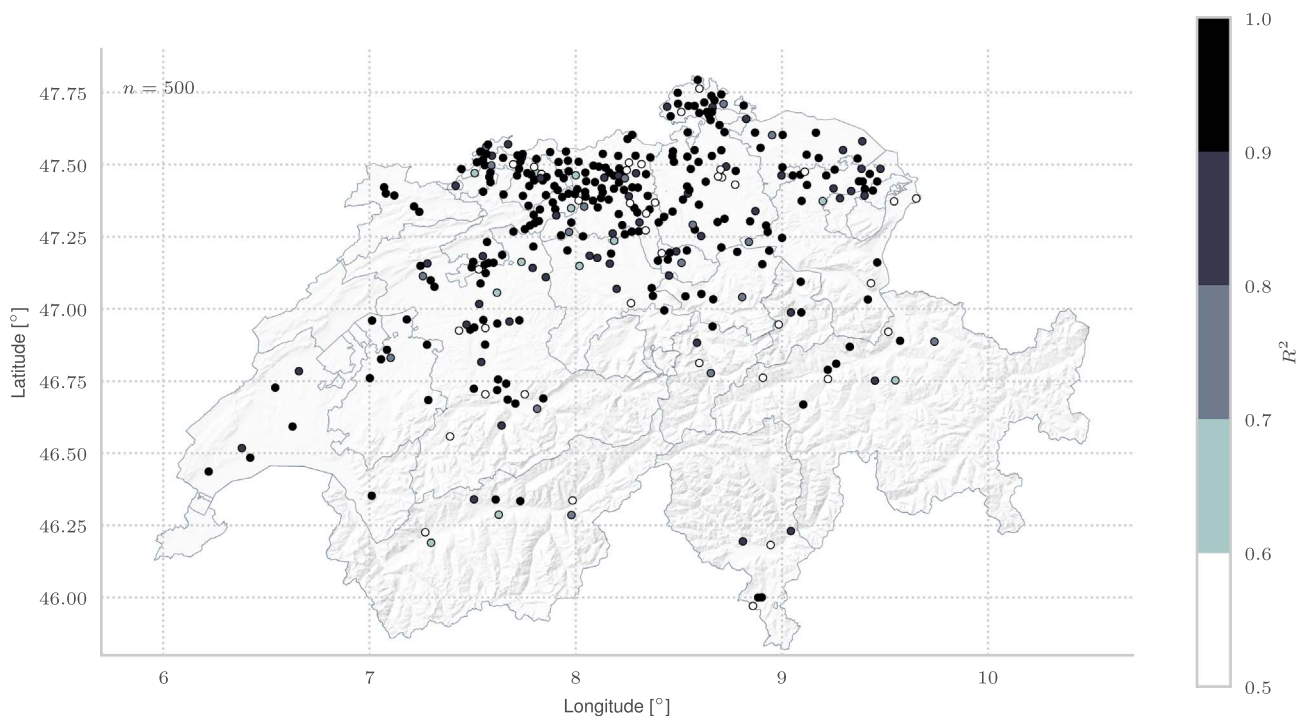


Fig. 10. Spatial distribution of goodness of fit (R^2) for the PV plants.

the penetration of a PV technology in the energy mix. Given a PV conversion efficiency, investment costs, electricity price and subsidies, a mean yearly irradiation threshold can be computed in order to estimate the profitability of plants. In Fig. 11a a selected value of the mean yearly irradiation on the x-axis corresponds to a value on the y-axis of the cumulative rooftop area with at least the selected mean yearly irradiation. Similarly in Fig. 11b, given a value of the mean yearly solar irradiation, the cumulative solar energy on rooftops can be identified. As an example for a selected threshold of at least $1000 \frac{\text{kWh}}{\text{m}^2}$ long-term mean irradiation, roughly 34,000 ha rooftop area with at least this level of irradiation are available. This area accumulates to roughly $400 \frac{\text{TWh}}{\text{year}}$ irradiation for the long-term mean scenario. With this information, policy makers are able to identify scenarios of PV production potentials based on the rooftop area and its solar irradiation potential.

5. Discussion

In this paper, we propose a method to estimate the monthly solar irradiation potential on building rooftops using GIS and spatio-temporal climate data from the CM SAF. Our method uses satellite solar irradiation data to derive typical daily solar irradiation profiles for each month in any given location with a 30-min resolution. We map an interval of solar irradiation potential for each rooftop in Switzerland using these daily profiles in combination with a digital surface model (DSM) that represents the objects on the bare ground and building footprints. To evaluate the accuracy of our result, we also validate our findings by comparing the monthly electricity production of 500 PV plants located in Switzerland with our electricity estimates using a customized PV model.

5.1. Scalability

Estimating solar irradiation potential of large regions bottom-up is a challenging task due to the considerable amount of data necessary to

carry out complex computations. Our method uses simplifications (in the form of typical monthly profiles) to reduce the computational complexity and to exploit multi-processing and a distributed processing infrastructure. These simplifications result in faster computations and efficiency. Precomputed solar irradiances for inclined surfaces with different angles of slope and orientations are computed only once and can be reused for multiple buildings. This reduces the number of frequently required complex computations. In addition, the use of monthly profiles also allows us to model the effect of shadowing with a half-hour resolution while removing the need to calculate every day of a year. Furthermore, each of the three phases presented in Fig. 1 can be parallelized or distributed among different computers. In the first phase, the monthly profiles of each cell can be computed independently whereas in phase two different partitions of the DSM can be processed independently. Finally, in the third phase, all buildings within the same cell of the solar irradiation dataset use the same monthly profiles, thus processing of the buildings can be partitioned by the cells of the solar dataset. We ran the computations alternatively on a virtual machine (VMWARE vSphere) running Linux on a host with two Intel(R) Xeon(R) E5-2680 v4 CPUs (each with 14 cores, respectively 28 threads) and 128 GB of RAM as well as a self-made cluster out of 9 computers of our students computer lab. Each of these computers has a Intel(R) Xeon(R) CPU E31240 CPU (each with 4 cores, respectively 8 threads) and 16 GB of RAM. The processing time of one building using the precomputed horizon, slope, orientation datasets, and the daily profiles is typically below two seconds, although buildings with a large footprint area can take longer ($\mathcal{O}(n)$, n = number of cells within building footprint). The workflow is implemented using Python and different open source libraries, such as rasterio, fiona, shapely, rtree and dispy as well as GRASS GIS. Computationally intensive parts of the Python code are optimized using the Cython framework.

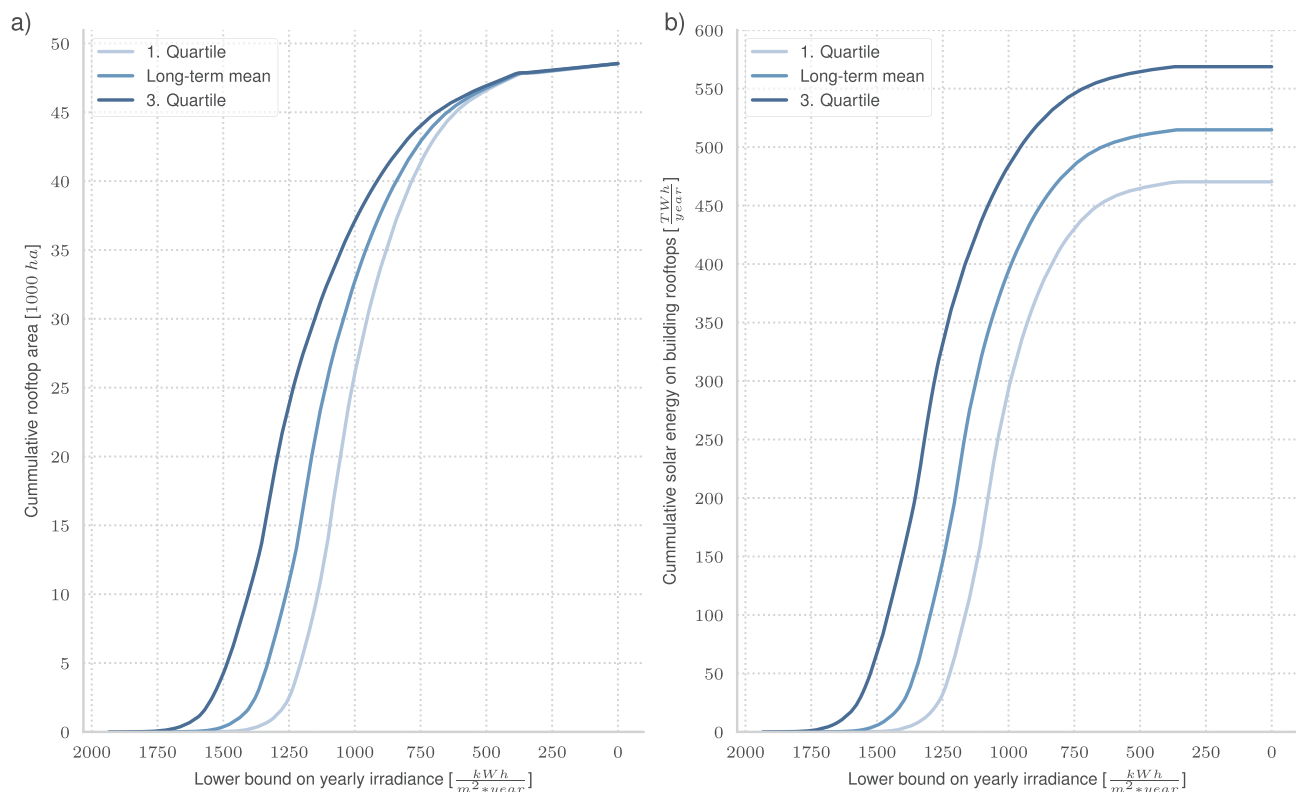


Fig. 11. (a) Cumulative available roof area with at least the selected yearly irradiation. (b) Cumulative solar irradiation on building rooftops for different levels of mean yearly irradiances.

5.2. Uncertainties

Naturally, the quality of the results is bound by the quality of the used datasets and models. Especially over complex terrains, such as in mountains, the spatial resolution can lead to uncertainties in the estimates. The validation of the CM SAF dataset for Switzerland [46] revealed a systematic error for the winter months at elevations corresponding to mountainous terrain. However, as most of the buildings, and thus the rooftop area in Switzerland, are located at lower elevations, the impact on the countrywide estimates is small.

Our validation shows during winter months an overestimation of the electricity production. However, as most of the solar irradiation is accumulated over the rest of the year, the impact is small. A logical explanation for this phenomenon is soiling through snow cover, which could also be the reason for the missing validation data in the same period. However this cannot be verified with the used datasets.

Next to solar irradiation, the quality of the DSM influences the uncertainty of our estimates. While the building footprints datasets are updated continuously, the creation of a DSM requires costly investments and is done over much longer intervals. Where possible, we used the most current available data. Nevertheless, changes of buildings, such as modifications or new constructions, cannot be modelled after the creation of the used DSMs. The next version of a complete DSM of Switzerland is not expected to be available before 2022. In addition, the accuracy of the building footprints influences the estimates. While the vast majority of the used building footprints are highly accurate, we had to rely on a small percentage of footprints with a lower quality.

While the validation showed very strong results, uncertainties remain due to available PV plants in the validation dataset. For example, only a small percentage of panels have a slope greater than 50° or face north. Thus, we were not able to verify our model for these conditions. In addition, as the exact location of the PV plants was unknown, we have no information about potential shadowing of PV panels in the validation dataset. As we assumed for the validation that no panel is shadowed, we were not able to test the accuracy of our shadowing model. The description of the components of the PV systems are user generated content. As we were not in possession of the exact plant location (only the ZIP code area), we had no means to verify the quality of, for example, the number of panels or their orientation and slope.

5.3. Applications

In Switzerland, nuclear power plants are expected to be phased out. This will reshape the Swiss electricity supply. The *Energy Strategy 2050*, formulated by the Swiss government, foresees an increase of renewable energy production by 14.5 TWh up to 2035 [66]. PV is expected to have the highest contribution to this increased share of renewables. Yet, it is unclear where and with what capacity additional PV plants will be installed. Our results will help homeowners to identify whether their rooftop area is suitable for the installation of PV panels. Aside of electricity generation, solar energy can be used to provide warm water and heat. In combination with building heat demand models, which are already available for Switzerland [39], the model can be used to analyse the energy saving potentials of solar based heating systems. On a larger scale, utilities face the challenge that the share of PV increases (see Appendix A) while little is known about the future spatio-temporal distribution of the PV generation. Modifications of the power grid are costly and can take a long time to plan, this impedes utilities to optimize their power grids for the integration of an increased PV supply in a cost-efficient manner. Previously, the relationship between available rooftop area and solar irradiance was unknown. Thus, policymakers were required to design their policies on assumptions not based on spatio-temporal explicit models. This allows policy makers to analyze the solar potential based on actual available rooftop area.

5.4. Data availability and limitations

In our model, we only consider PV modules that are directly mounted on the rooftop, thus having the same slope and orientation as the underlying roof. However, especially on flat roofs, PV modules can also be mounted on racks and oriented at a more optimal angle and orientation to the sun. This is a limitation of our current modelling approach. Future research can consider the optimal orientation (both for aspect and slope) of panels on flat roofs by means of maximizing the incoming solar irradiation. Furthermore, we do not model solar tracking technology that aligns PV panels during the day optimally towards the sun. As a result, we underestimate the solar irradiation when these technologies are used.

A further limitation of our model is the dependency on accurate DSM models. Although the creation of DSM models using LIDAR is expensive, several countries exist that have a complete coverage of LIDAR data (Finland, Netherlands, Slovenia) or are in the process of doing so (Latvia, Poland, Spain, Sweden, England) [67]. An alternative to DSMs are 3D building models. As Google maps(TM) demonstrates, it is not unrealistic that worldwide 3D buildings models, created from aerial photos, will be available in the near future. Without DSM or 3D building models, it is not possible to identify the PV suitable rooftop area of individual building. However, if one is only interested in aggregated estimates, the use of statistical methods [68] is an option.

In contrast weather satellites have a near worldwide coverage. Thus, a large share of the inhabited places on earth are covered by satellite irradiation datasets. While the CMSAF SAHRAH solar dataset covers most of Europe and Africa, similar datasets exists for other parts of the world (e.g., for North America [69]).

6. Conclusion

Our simulations show that the long-term mean potential of solar irradiation on building rooftops in Switzerland is in the range of the yearly-consumed domestic energy. In the specific case of Switzerland, the PV solar irradiation potential on rooftops is important because it represents the largest additional potential renewable contribution to replace the missing electricity generation due to the phasing out of nuclear power plants. Furthermore, the spatio-temporal modelling of the solar potential allows utilities to plan their future power grids for the integration of an increased share of PV production.

Currently, PV adoption scenarios for Switzerland do not rely on spatially explicit models. As it is possible with our method to simulate the solar irradiation potential for each building, we were able to identify the relationship between yearly solar irradiance levels and available rooftop area. This will help to increase the robustness of PV adoption scenarios.

Previous work has focused on average annual or monthly estimates of the solar irradiation on building rooftops. This neglects the variability between different years due to, for example, different cloud patterns or snow cover. This is important information for multiple purposes in different domains and applications such as energy policy strategies, identification rooftops for PV plants, optimal integration of PV into the existing distribution grid, and the spatio-temporal impact of PV plants on the grid itself. In addition, most of PV plants are installed on building rooftops and feed into the distribution grid; therefore, the usage of the interval of the potential solar irradiation, and thus electricity generation, allows us to generate different scenarios for future sustainable urban planning powered by smart distribution grids with integrated energy storage. Solar energy is predicted to make a major contribution to the energy supply due to its flexibility of installation, its relatively easy maintenance, decreasing costs, and the improvement of its technical performance. When considering large integrated energy systems, it is critical and fundamental to assess the spatio-temporal availability of renewable energy resources in order to optimize both their generation and dispatch and the planning future storage systems.

Our study area is by orders of magnitude larger compared to other studies modelling the solar potential based on LIDAR data. While previous studies considered small urban regions, we simulate a whole country of the size of 41,285 km² with a building footprint area of in total 48,536 ha. This is possible due to the scalability of our method, achieved by computing expensive calculations only once and exploiting multiprocessing environments.

While our model calculates an upper bound of the solar potential on building rooftops, more research needs to be conducted to model PV adoption rate scenarios. For example, we do not model the economic aspects of PV systems or social and regulatory factors relevant for the

installation of PV plants. Such a techno-economic analysis is out of scope of this work and will be pursued in future research.

Acknowledgments

René Buffat is funded by the Commission for Technology and Innovation (CTI) within the Swiss Competence Center for Energy Research (SCCER) FURIES (Future Swiss Electrical Infrastructure). The authors of this paper would like to thank Lorenz Schmid and Tobias Duewell for helping with the data matching process.

Appendix A. Capacity factor for Switzerland

The Swiss Federal Office of Energy publishes since 2011 yearly a list of all subsidized PV plants [72–74]. This list includes for each plant the date of the initial operation, the installed capacity of the plant, and the production of the plant in the corresponding year. Table A.1 shows for each year of production the mean capacity factor of all plants operating the full year (respectively having an initial date of operation before the year of the production). Averaging the yearly factors results in a mean capacity factor of 10.33%.

Table A.1

Capacity factors of Swiss PV plants for different years of production.

Production year	Number of yearly plant production values	Mean capacity factor
2011	2195	10.17
2012	3811	10.67
2013	5727	9.66
2014	7831	9.57
2015	9948	11.43
2016	11,299	10.47
2011–2016	40,811	10.33

References

- [1] Myers DR. Solar radiation modeling and measurements for renewable energy applications: data and model quality. *Energy* 2005;30(9):1517–31. <http://dx.doi.org/10.1016/j.energy.2004.04.034>.
- [2] Stoffel T. Chapter 1 – terms and definitions. In: Kleissl J, editor. *Solar energy forecasting and resource assessment* Boston: Academic Press; 2013. p. 1–19. <http://dx.doi.org/10.1016/B978-0-12-397177-7.00001-2>. URL <<https://www.sciencedirect.com/science/article/pii/B9780123971777000012>> .
- [3] Jordan DC, Kurtz SR, VanSant K, Newmiller J. Compendium of photovoltaic degradation rates. *Prog Photovoltaics: Res Appl* 2016;24(7):978–89. <http://dx.doi.org/10.1002/pip.2744>. URL pIP-15-244.R1.
- [4] Cano D, Monget J, Albuissou M, Guillard H, Regas N, Wald L. A method for the determination of the global solar radiation from meteorological satellite data. *Sol Energy* 1986;37(1):31–9. [http://dx.doi.org/10.1016/0038-092x\(86\)90104-0](http://dx.doi.org/10.1016/0038-092x(86)90104-0).
- [5] Lu N, Qin J, Yang K, Sun J. A simple and efficient algorithm to estimate daily global solar radiation from geostationary satellite data. *Energy* 2011;36(5):3179–88. <http://dx.doi.org/10.1016/j.energy.2011.03.007>.
- [6] Müller R, Pfeifroth U, Träger-Chatterjee C, Trentmann J, Cremer R. Digging the METEOSAT treasure—3 decades of solar surface radiation. *Rem Sens* 2015;7(6):8067–101. <http://dx.doi.org/10.3390/rs70608067>. URL <<http://www.mdpi.com/2072-4292/7/6/8067>> .
- [7] Hulme M, Conway D, Jones PD, Jiang T, Barrow EM, Turney C. Construction of a 1961–1990 European climatology for climate change modelling and impact applications. *Int J Climatol* 1995;15(12):1333–63. <http://dx.doi.org/10.1002/joc.3370151204>.
- [8] Hutchinson M, Booth T, McMahon J, Nix H. Estimating monthly mean values of daily total solar radiation for Australia. *Sol Energy* 1984;32(2):277–90. [http://dx.doi.org/10.1016/S0038-092x\(84\)80045-6](http://dx.doi.org/10.1016/S0038-092x(84)80045-6).
- [9] Zelenka A, Czeplak G, D'Agostino V. Techniques for supplementing solar radiation network data: report. International Energy Agency; 1992.
- [10] Neteler M, Mitasova H. *Open source GIS: a GRASS GIS approach* (Kluwer International Series in Engineering and Computer Science). 1st ed. Springer; 2002.
- [11] Hofierka J. Direct solar radiation modelling within an open GIS environment. In: *Proceedings of JEC-GI'97 conference in Vienna, Austria*, IOS Press Amsterdam; 1997. p. 575–84.
- [12] Rigollier C, Bauer O, Wald L. On the clear sky model of the ESRA – European Solar Radiation Atlas – with respect to the heliosat method. *Sol Energy* 2000;68(1):33–48. [http://dx.doi.org/10.1016/S0038-092x\(99\)00055-9](http://dx.doi.org/10.1016/S0038-092x(99)00055-9).
- [13] Koo C, Hong T, Lee M, Park HS. Estimation of the monthly average daily solar radiation using geographic information system and advanced case-based reasoning. *Environ Sci Technol* 2013;47(9):4829–39. <http://dx.doi.org/10.1021/es303774a>.
- [14] wei Sun Y, Hof A, Wang R, Liu J, jie Lin Y, wei Yang D. GIS-based approach for potential analysis of solar PV generation at the regional scale: a case study of Fujian Province. *Energy Policy* 2013;58:248–59. <http://dx.doi.org/10.1016/j.enpol.2013.03.002>.
- [15] Suomalainen K, Wang V, Sharp B. Rooftop solar potential based on lidar data: Bottom-up assessment at neighbourhood level. *Renew Energy* 2017;111:463–75. <http://dx.doi.org/10.1016/j.renene.2017.04.025>. URL <<http://www.sciencedirect.com/science/article/pii/S0960148117303324>> .
- [16] Ruiz-Arias JA, Quesada-Ruiz S, Fernández EF, Gueymard CA. Optimal combination of gridded and ground-observed solar radiation data for regional solar resource assessment. *Sol Energy* 2015;112:411–24. <http://dx.doi.org/10.1016/j.solener.2014.12.011>.
- [17] Ineichen P. Five satellite products deriving beam and global irradiance validation on data from 23 ground stations; 2011. p. 333.7–9. iD: unige:23669. URL <<http://archive-ouverte.unige.ch/unige:23669>> .
- [18] Peng J, Lu L. Investigation on the development potential of rooftop PV system in Hong Kong and its environmental benefits. *Renew Sustain Energy Rev* 2013;27:149–62. <http://dx.doi.org/10.1016/j.rser.2013.06.030>.
- [19] Karteris M, Slini T, Papadopoulos A. Urban solar energy potential in Greece: a statistical calculation model of suitable built roof areas for photovoltaics. *Energy Build* 2013;62:459–68. <http://dx.doi.org/10.1016/j.enbuild.2013.03.033>.
- [20] Bergamasco L, Asinari P. Scalable methodology for the photovoltaic solar energy potential assessment based on available roof surface area: application to Piedmont Region (Italy). *Sol Energy* 2011;85(5):1041–55. <http://dx.doi.org/10.1016/j.solener.2011.02.022>.
- [21] Schallenberg-Rodríguez J. Photovoltaic techno-economical potential on roofs in regions and islands: the case of the Canary Islands. Methodological review and methodology proposal. *Renew Sustain Energy Rev* 2013;20:219–39. <http://dx.doi.org/10.1016/j.rser.2012.11.078>.
- [22] Buffat R. Feature-aware surface interpolation of rooftops using low-density lidar data for photovoltaic applications. Springer International Publishing, Cham; 2016. p. 337–50. http://dx.doi.org/10.1007/978-3-319-33783-8_19.
- [23] Lingfors D, Bright J, Engerer N, Ahlberg J, Killinger S, Widén J. Comparing the capability of low- and high-resolution LIDAR data with application to solar resource assessment, roof type classification and shading analysis. *Appl Energy* 2017;205(Suppl C):1216–30. <http://dx.doi.org/10.1016/j.apenergy.2017.08.045>. URL <<http://www.sciencedirect.com/science/article/pii/S0306261917310619>> .
- [24] Hong T, Lee M, Koo C, Jeong K, Kim J. Development of a method for estimating the rooftop solar photovoltaic (PV) potential by analyzing the available rooftop area using Hillshade analysis. *Appl Energy* 2017;194:320–32. <http://dx.doi.org/10.1016/j.apenergy.2016.07.001>. URL <<http://www.sciencedirect.com/science/article/pii/S0306261916309424>> .
- [25] Lukač N, Žlaus D, Seme S, Žalik B, Štumberger G. Rating of roofs' surfaces regarding

- their solar potential and suitability for PV systems, based on LiDAR data. *Appl Energy* 2013;102(Suppl C):803–12. <http://dx.doi.org/10.1016/j.apenergy.2012.08.042> URL Special issue on advances in sustainable biofuel production and use – XIX international symposium on alcohol fuels – ISAF <<http://www.sciencedirect.com/science/article/pii/S0306261912006162>> .
- [26] Carneiro C, Morello E, Desthieux G. Assessment of solar irradiance on the urban fabric for the production of renewable energy using LiDAR data and image processing techniques. Berlin (Heidelberg): Springer Berlin Heidelberg; 2009. p. 83–112. http://dx.doi.org/10.1007/978-3-642-00318-9_5.
- [27] Gooding J, Crook R, Tomlin AS. Modelling of roof geometries from low-resolution LiDAR data for city-scale solar energy applications using a neighbouring buildings method. *Appl Energy* 2015;148:93–104. <http://dx.doi.org/10.1016/j.apenergy.2015.03.013>.
- [28] Jacques DA, Gooding J, Giesekam JJ, Tomlin AS, Crook R. Methodology for the assessment of PV capacity over a city region using low-resolution LiDAR data and application to the City of Leeds (UK). *Appl Energy* 2014;124:28–34. <http://dx.doi.org/10.1016/j.apenergy.2014.02.076>.
- [29] Santos T, Gomes N, Freire S, Brito M, Santos L, Tenedório J. Applications of solar mapping in the urban environment. *Appl Geogr* 2014;51:48–57. <http://dx.doi.org/10.1016/j.apgeog.2014.03.008>.
- [30] Li Y, Ding D, Liu C, Wang C. A pixel-based approach to estimation of solar energy potential on building roofs. *Energy Build* 2016;129:563–73. <http://dx.doi.org/10.1016/j.enbuild.2016.08.025>. URL <<http://www.sciencedirect.com/science/article/pii/S0378778816307101>> .
- [31] Rodríguez LR, Duminiel E, Ramos JS, Eicker U. Assessment of the photovoltaic potential at urban level based on 3D city models: a case study and new methodological approach. *Sol Energy* 2017;146:264–75. <http://dx.doi.org/10.1016/j.solener.2017.02.043>. URL <<http://www.sciencedirect.com/science/article/pii/S0038092X17301445>> .
- [32] Pili S, Desogus G, Melis D. A gis tool for the calculation of solar irradiation on buildings at the urban scale, based on Italian standards. *Energy Build* 2018;158:629–46. <http://dx.doi.org/10.1016/j.enbuild.2017.10.027>. URL <<http://www.sciencedirect.com/science/article/pii/S0378778817314962>> .
- [33] Lorenz E, Hurka J, Heinemann D, Beyer HG. Irradiance forecasting for the power prediction of grid-connected photovoltaic systems. *IEEE J Sel Top Appl Earth Obs Rem Sens* 2009;2(1):2–10. <http://dx.doi.org/10.1109/jstars.2009.2020300>.
- [34] Lorenz E, Scheidsteger T, Hurka J, Heinemann D, Kurz C. Regional PV power prediction for improved grid integration. *Prog Photovolt: Res Appl* 2010;19(7):757–71. <http://dx.doi.org/10.1002/ppp.1033>.
- [35] Grover-Silva E, Girard R, Kariniotakis G. Optimal sizing and placement of distribution grid connected battery systems through an SOCP optimal power flow algorithm. *Appl Energy*. <http://dx.doi.org/10.1016/j.apenergy.2017.09.008>. URL <<http://www.sciencedirect.com/science/article/pii/S0306261917312813>> .
- [36] Strzalka A, Alam N, Duminiel E, Coors V, Eicker U. Large scale integration of photovoltaics in cities. *Appl Energy* 2012;93(Suppl C):413–21 [(1) Green energy; (2) special section from papers presented at the 2nd international energy 2030 conf]. <http://dx.doi.org/10.1016/j.apenergy.2011.12.033>. URL <<http://www.sciencedirect.com/science/article/pii/S0306261911008294>> .
- [37] Cole W, Lewis H, Sigrin B, Margolis R. Interactions of rooftop PV deployment with the capacity expansion of the bulk power system. *Appl Energy* 2016;168(Suppl C):473–81. <http://dx.doi.org/10.1016/j.apenergy.2016.02.004>. URL <<http://www.sciencedirect.com/science/article/pii/S0306261916301271>> .
- [38] Buffat R, Bucher D, Raubal M. Using locally produced photovoltaic energy to charge electric vehicles. *Comput Sci – Res Dev*. <http://dx.doi.org/10.1007/s00450-017-0345-8>.
- [39] Buffat R, Froemelt A, Heeren N, Raubal M, Hellweg S. Big data GIS analysis for novel approaches in building stock modelling. *Appl Energy* 2017;208:277–90. <http://dx.doi.org/10.1016/j.apenergy.2017.10.041>. URL <<http://www.sciencedirect.com/science/article/pii/S030626191731454X>> .
- [40] Arnette AN. Integrating rooftop solar into a multi-source energy planning optimization model. *Appl Energy* 2013;111(Suppl C):456–67. <http://dx.doi.org/10.1016/j.apenergy.2013.05.003>. URL <<http://www.sciencedirect.com/science/article/pii/S0306261913003929>> .
- [41] Jakubiec JA, Reinhart CF. A method for predicting city-wide electricity gains from photovoltaic panels based on lidar and gis data combined with hourly dayism simulations. *Sol Energy* 2013;93:127–43. <http://dx.doi.org/10.1016/j.solener.2013.03.022>. URL <<http://www.sciencedirect.com/science/article/pii/S0038092X13001291>> .
- [42] Das Eidgenössische Departement für Verteidigung, Bevölkerungsschutz und Sport. Technische Verordnung des VBS über die amtliche Vermessung; July 2008.
- [43] Fan H, Zipf A, Fu Q, Neis P. Quality assessment for building footprints data on openstreetmap. *Int J Geogr Inform Sci* 2014;28(4):700–19. <http://dx.doi.org/10.1080/13658816.2013.867495>.
- [44] Bundesamt für Statistik. Arealstatistik: Land Cover 2004/09; October 2016.
- [45] Richard Müller and Uwe Pfeifroth and Christine Träger-Chatterjee and Roswitha Cremer and Jörg Trentmann and Rainer Hollmann. Surface solar radiation data set – heliosat (SARAH) – edition 1; 2015. http://dx.doi.org/10.5676/EUM.SAF_CM/SARAH/V001.
- [46] Buffat R, Grassi S. Validation of CM SAF SARAH solar radiation datasets for Switzerland. In: 2015 3rd International renewable and sustainable energy conference (IRSEC); 2015. p. 1–6. <http://dx.doi.org/10.1109/IRSEC.2015.7455044>.
- [47] Duffie JA, Beckman WA. Solar engineering of thermal processes. Wiley-Blackwell; 2013. <http://dx.doi.org/10.1002/9781118671603>.
- [48] Reda I, Andreas A. Solar position algorithm for solar radiation applications. *Sol Energy* 2004;76(5):577–89. <http://dx.doi.org/10.1016/j.solener.2003.12.003>. URL <<http://www.sciencedirect.com/science/article/pii/S0038092X0300450X>> .
- [49] Yadav AK, Chandel S. Tilt angle optimization to maximize incident solar radiation: a review. *Renew Sustain Energy Rev* 2013;23:503–13. <http://dx.doi.org/10.1016/j.rser.2013.02.027>. URL <<http://www.sciencedirect.com/science/article/pii/S1364032113001299>> .
- [50] Demain C, Journée M, Bertrand C. Evaluation of different models to estimate the global solar radiation on inclined surfaces. *Renew Energy* 2013;50:710–21. <http://dx.doi.org/10.1016/j.renene.2012.07.031>. URL <<http://www.sciencedirect.com/science/article/pii/S0960148112004570>> .
- [51] Demain C, Journée M, Bertrand C. Corrigendum to Evaluation of different models to estimate the global solar radiation on inclined surfaces [Renew Energy 50 (2013) 710–721]. *Renew Energy* 2017;101:1401–3. <http://dx.doi.org/10.1016/j.renene.2016.07.041>. URL <<http://www.sciencedirect.com/science/article/pii/S0960148116306371>> .
- [52] Perez R, Ineichen P, Seals R, Michalsky J, Stewart R. Modeling daylight availability and irradiance components from direct and global irradiance. *Sol Energy* 1990;44(5):271–89. [http://dx.doi.org/10.1016/0038-092X\(90\)90055-H](http://dx.doi.org/10.1016/0038-092X(90)90055-H). URL <<http://www.sciencedirect.com/science/article/pii/S0038092X9000555H>> .
- [53] Soto WD, Klein S, Beckman W. Improvement and validation of a model for photovoltaic array performance. *Sol Energy* 2006;80(1):78–88. <http://dx.doi.org/10.1016/j.solener.2005.06.010>. URL <<http://www.sciencedirect.com/science/article/pii/S0038092X05002410>> .
- [54] Shannan NMAA, Yahaya NZ, Singh B. Single-diode model and two-diode model of pv modules: a comparison. In: 2013 IEEE international conference on control system, computing and engineering; 2013. p. 210–4. <http://dx.doi.org/10.1109/ICCSCE.2013.6719960>.
- [55] Singh G. Solar power generation by PV (photovoltaic) technology: a review. *Energy* 2013;53:1–13. <http://dx.doi.org/10.1016/j.energy.2013.02.057>. URL <<http://www.sciencedirect.com/science/article/pii/S036051423001758>> .
- [56] Batzelis EI, Georgilakis PS, Papathanassiou SA. Energy models for photovoltaic systems under partial shading conditions: a comprehensive review. *IET Renew Power Gener* 2015;9(4):340–9. <http://dx.doi.org/10.1049/iet-rpg.2014.0207>.
- [57] Batzelis EI, Papathanassiou SA. A method for the analytical extraction of the single-diode PV model parameters. *IEEE Trans Sustain Energy* 2016;7(2):504–12. <http://dx.doi.org/10.1109/TSTE.2015.2503435>.
- [58] Tian H, Mancilla-David F, Ellis K, Muljadi E, Jenkins P. A cell-to-module-to-array detailed model for photovoltaic panels. *Sol Energy* 2012;86(9):2695–706. <http://dx.doi.org/10.1016/j.solener.2012.06.004>. URL <<http://www.sciencedirect.com/science/article/pii/S0038092X12002150>> .
- [59] Batzelis EI, Kampitsis GE, Papathanassiou SA, Manias SN. Direct MPP calculation in terms of the single-diode PV model parameters. *IEEE Trans Energy Convers* 2015;30(1):226–36. <http://dx.doi.org/10.1109/TEC.2014.2356017>.
- [60] Nelson J. The physics of solar cells (properties of semiconductor materials). Imperial College Press; 2003.
- [61] Dobos AP. PVWatts version 5 manual. National Renewable Energy Laboratory. September. URL <<https://www.nrel.gov/docs/fy14osti/62641.pdf>> .
- [62] W. Holmgren, Calama-Consulting, T. Lorenzo, Bmu, Ukrien, DaCoEx, Mayudong, E. Miller, Jforbess. PyElena21. L. T. pvlbi-python: 0.3.1; 2016. <http://dx.doi.org/10.5281/zenodo.50141>.
- [63] Kymakis E, Kalykakis S, Papazoglou TM. Performance analysis of a grid connected photovoltaic park on the island of Crete. *Energy Convers Manage* 2009;50(3):433–8. <http://dx.doi.org/10.1016/j.enconman.2008.12.009>. URL <<http://www.sciencedirect.com/science/article/pii/S0196890408004615>> .
- [64] Pfenninger S, Staffell I. Long-term patterns of European PV output using 30 years of validated hourly reanalysis and satellite data. *Energy* 2016;114:1251–65. <http://dx.doi.org/10.1016/j.energy.2016.08.060>. URL <<http://www.sciencedirect.com/science/article/pii/S0306544216311744>> .
- [65] Bundesamt für Energie BFE. Schweizerische Gesamtenergiestatistik 2015; July 2016.
- [66] Eidgenössisches Departement für Umwelt, Verkehr, Energie und Kommunikation UVEK. Faktenblatt Energie sparen und Energieeffizienz erhöhen; March 2017.
- [67] Wikipedia. National lidar dataset – wikipedia, the free encyclopedia [Online; accessed 11-January-2018]; 2018. URL <http://en.wikipedia.org/w/index.php?title=National_lidar_dataset&oldid=818854673> .
- [68] Gagnon P, Margolis R, Melius J, Phillips C, Elmore R. Estimating rooftop solar technical potential across the u.s. using a combination of gis-based methods, lidar data, and statistical modeling. *Environ Res Lett*. URL <<http://iopscience.iop.org/10.1088/1748-9326/aaa554>> .
- [69] Perez R, Ineichen P, Moore K, Kmiecik M, Chain C, George R, et al. A new operational model for satellite-derived irradiances: description and validation. *Sol Energy* 2002;73(5):307–17. [http://dx.doi.org/10.1016/S0038-092X\(02\)00122-6](http://dx.doi.org/10.1016/S0038-092X(02)00122-6). URL <<http://www.sciencedirect.com/science/article/pii/S0038092X02001226>> .
- [70] Swiss Federal Office of Energy. Liste aller KEV-Bezüger im Jahr 2011; 4, 2014. URL <[http://www.bfe.admin.ch/php/modules/publikationen/stream.php?extlang=de&name=de_913889099.pdf&endung=Evaluation%20der%20kostendeckenden%20Einspeiseverg&FCtung%20\(KEV\)](http://www.bfe.admin.ch/php/modules/publikationen/stream.php?extlang=de&name=de_913889099.pdf&endung=Evaluation%20der%20kostendeckenden%20Einspeiseverg&FCtung%20(KEV))> .
- [71] Swiss Federal Office of Energy. Liste aller KEV-Bezüger im Jahr 2012; 4, 2014. URL <http://www.bfe.admin.ch/php/modules/publikationen/stream.php?extlang=de&name=de_378876214.xlsx&endung=Liste%20aller%20KEV-Bez%FCger%20im%20Jahr%202012> .
- [72] Swiss Federal Office of Energy. Liste aller KEV-Bezüger im Jahr 2013; 4, 2014. URL <http://www.bfe.admin.ch/php/modules/publikationen/stream.php?extlang=de&name=de_749247011.xlsx&endung=Liste%20aller%20KEV-Bez%FCger%20im%20Jahr%202013> .
- [73] Swiss Federal Office of Energy. Liste aller KEV-Bezüger im Jahr 2014; 5, 2015. URL <http://www.bfe.admin.ch/php/modules/publikationen/stream.php?extlang=de&name=de_502661552.xlsx&endung=Liste%20aller%20KEV-Bez%FCger%20im%20Jahr%202014> .
- [74] Swiss Federal Office of Energy. Liste aller KEV-Bezüger im Jahr 2015; 5, 2016. URL <http://www.bfe.admin.ch/php/modules/publikationen/stream.php?extlang=de&name=de_58802254.xlsx&endung=Liste%20aller%20KEV-Bez%FCger%20im%20Jahr%202015> .